

# Analytical modeling and experimental validation of a structurally integrated piezoelectric energy harvester on a thin plate

U Aridogan<sup>1</sup>, I Basdogan<sup>1</sup> and A Erturk<sup>2</sup>

<sup>1</sup> Department of Mechanical Engineering, College of Engineering, Koç University, Istanbul, 34450, Turkey

<sup>2</sup> G W Woodruff School of Mechanical Engineering, Georgia Institute of Technology, Atlanta, GA 30332, USA

E-mail: [ibasdogan@ku.edu.tr](mailto:ibasdogan@ku.edu.tr)

Received 24 July 2013, revised 13 December 2013

Accepted for publication 7 January 2014

Published 13 March 2014

## Abstract

Vibration-based energy harvesting using piezoelectric cantilevers has been extensively studied over the past decade. As an alternative to cantilevered harvesters, piezoelectric patch harvesters integrated to thin plates can be more convenient for use in marine, aerospace and automotive applications since these systems are often composed of thin plate-like structures with various boundary conditions. In this paper, we present analytical electroelastic modeling of a piezoelectric energy harvester structurally integrated to a thin plate along with experimental validations. The distributed-parameter electroelastic model of the thin plate with the piezoceramic patch harvester is developed based on Kirchhoff's plate theory for all-four-edges clamped (CCCC) boundary conditions. Closed-form steady-state response expressions for coupled electrical output and structural vibration are obtained under transverse point force excitation. Analytical electroelastic frequency response functions (FRFs) relating the voltage output and vibration response to force input are derived and generalized for different boundary conditions. Experimental validation and extensive theoretical analysis efforts are then presented with a case study employing a thin PZT-5A piezoceramic patch attached on the surface of a rectangular aluminum CCCC plate. The importance of positioning of the piezoceramic patch harvester is discussed through an analysis of dynamic strain distribution on the overall plate surface. The electroelastic model is validated by a comparison of analytical and experimental FRFs for a wide range of resistive electrical boundary conditions. Finally, power generation performance of the structurally integrated piezoceramic patch harvester from multiple vibration modes is investigated analytically and experimentally.

Keywords: vibrational energy harvesting, piezoceramic patch-based harvesters, plate structures, electroelastic modeling, power output analysis

(Some figures may appear in colour only in the online journal)

## 1. Introduction

Vibration-based energy harvesting has been extensively studied for opportunities to develop self-powered, autonomous and wireless monitoring systems over the past two decades [1–3]. The transformation of vibration into electricity

has been achieved using electromagnetic [4, 5], electrostatic [6, 7], piezoelectric [8, 9], and magnetostrictive [10] conversion techniques, as well as the use of electroactive polymers [11]. Among these energy conversion alternatives, piezoelectric energy harvesting has attracted the greatest attention due to

high power density [12] and ease of fabrication of piezoelectric materials from submicron [8] to macro [9] scale.

The literature on piezoelectric energy harvesting has heavily focused on cantilever beams with piezoceramic layers due to their relative ease of implementation [9, 12]. Analytical and numerical electromechanical models of cantilever beam harvesters have been developed by several research groups [13–17]. Exact analytical distributed-parameter modeling [15], Rayleigh–Ritz solutions [16], and assumed-modes modeling [18] were presented for deterministic and random vibrations [19] with experimental verifications. Numerous studies focused on different aspects of cantilever beam harvesters. For instance, optimization for size and shape of piezoceramic layers [20], effects of strain distribution on electrical outputs [21], use of highly coupled materials [22] were studied. Novel mechanisms and configurations such as initial energy injection [23], array of harvesters [24], multi-dimensional operation [25] and buckled configurations [26, 27] have been proposed.

As compared to the number of studies dealing with piezoelectric harvester beams, research on plate-like piezoelectric energy harvesters has been very limited. De Marqui *et al* [28] presented an electromechanical finite element model (FEM) for a piezoelectric energy harvester embedded in a cantilever plate, and later on extended this FEM to airflow excitation problems by electroaeroelastic coupling [29, 30]. Rupp *et al* [31] conducted topology optimization studies for the distribution of piezoelectric material on cantilever plate and shell structures using FEM to maximize the harvested power. Erturk [32] derived analytical formulation for energy harvesting with piezoceramic patches from surface strain fluctuations of large and high impedance structures (such as concrete) through one-way coupling.

It is worth pointing out that research on piezoelectric energy harvesting followed the extensive research on piezoelectric shunt damping of structural vibration. Shunt damping and energy harvesting are associated with the aims of dissipating and extracting mechanical energy, respectively. The method of shunting the piezoelectric materials, which was initially proposed by Forward [33], employs connecting the electrodes of a piezoceramic layer to a passive circuit (which may include resistors, inductors, and capacitors) for the dissipation of vibration energy. Hagood and von Flotow [34] applied piezoelectric shunt damping to a cantilever beam, obtained a single-degree-of-freedom (SDOF) model and conducted experiments for the vibration suppression of the first mode of the beam. Hollkamp [35] extended SDOF modeling and experiments to multi-vibration modes of a cantilever beam by adding parallel branches including resistors, inductors and capacitors. Wu [36] developed current-blocking technique and showed that this technique can be used for the multi-mode shunt damping of the cantilever beams. An analytical formulation of a thin plate with surface-bonded piezoceramic transducer for active and passive damping was studied by Koshigoe and Murdock [37]. Saravanos [38] presented an analytical model of a simply supported multi-layered piezoceramic composite plate inside of which piezoceramic laminates are connected to a passive circuit. Behrens *et al* [39]

introduced current-flowing technique, which is similar to the current-blocking technique, to simplify the shunt circuit and performed numerical and experimental analysis on simply-supported plate. Fein [40] presented numerical and experimental analysis of piezoelectric shunt damping on a clamped plate with multiple piezoceramic patches and conducted an optimal placement study based on the effective strain energy method. As pointed out by Moheimani [41] in a review article, the requirement of large inductors limits the use of piezoelectric shunt damping at low frequencies and environmental variations significantly degrade performance. For these reasons, implementation of synthetic impedance [42] and online adaptation [43], simultaneous use of passive and active piezoelectric actuators [44, 45], periodic arrangement of shunted piezoceramic patches [46] have been suggested and developed for vibration energy dissipation of thin plates. Recently, the two research areas of energy harvesting and vibration control have been considered together for the purpose of self-powered vibration control systems, which are referred to as energy recycling [47]. However energy harvesting capabilities of integrated piezoceramic materials on thin plates have not been addressed.

This paper presents analytical electroelastic modeling and experimental validations of piezoceramic patch-based energy harvesters structurally integrated on thin plates. The motivation for choosing flexible thin plates as host structures is their common use in a wide variety of engineering structures and systems, where piezoceramic patches can easily be attached for vibration-based energy harvesting (whereas a cantilever can modify the host system dynamics). A reliable analytical model for energy harvesting from thin plates employing integrated patches can be used in design, performance prediction and power output optimization. To this end, in the following sections, a distributed-parameter electroelastic model of a thin plate with a piezoceramic patch harvester is developed based on Kirchhoff's plate theory and modal analysis solution (in the same vein as the electroelastic beam model by Erturk and Inman [15]). Closed-form steady-state solutions for electrical and structural responses are obtained for harmonic force excitation. Multi-mode and single-mode analytical frequency response functions (FRFs) between voltage output-to-force input and displacement-to-force input are derived and generalized for different boundary conditions of thin plates. A case study is presented for the experimental validation of harvester performance. The dynamic strain distribution of a CCCC plate is discussed with an emphasis on vibration-mode-dependent preferred locations of piezoelectric patch for effective energy harvesting. Experimental and analytical FRFs are then compared for a wide range of resistive electrical loads to show the accuracy of the analytical electroelastic model. Finally, energy harvesting from multiple vibration modes is analyzed extensively using analytical and experimental results.

## 2. Distributed-parameter electroelastic modeling

### 2.1. Governing electroelastic equations in physical coordinates

In figure 1, a piezoelectric energy harvester in the form of a thin piezoceramic patch (small plate) is structurally integrated

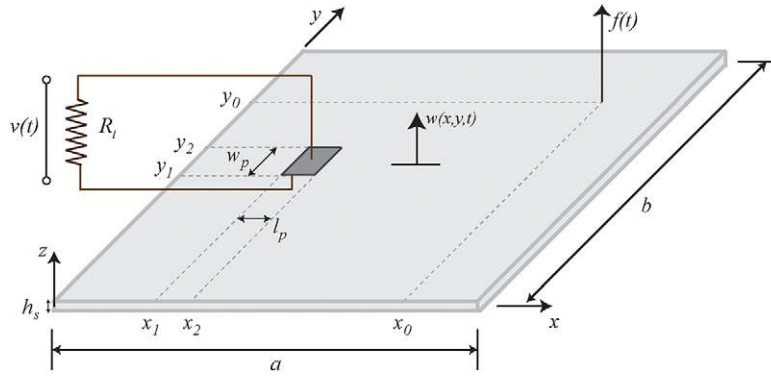


**Figure 1.** Piezoelectric energy harvesting using a patch structurally integrated on a thin plate under transverse force excitation.

to a large host plate, which is excited by a transverse point force  $f(t)$  acting at the position coordinates  $(x_0, y_0)$ . The geometrically uniform plate is assumed to be thin so that the effects of transverse shear deformation are neglected based on the Kirchhoff plate theory. A perfectly bonded transversely isotropic piezoceramic patch with a length of  $l_p$  and width of  $w_p$  covers a rectangular region with two corners at  $(x_1, y_1)$  and  $(x_2, y_2)$ . The length and width of the host plate are  $a$  and  $b$ , respectively. Thicknesses of the host plate and the piezoceramic patch are  $h_s$  and  $h_p$ , respectively. A resistive load ( $R_l$ ) is considered as an external electrical load connected to the perfectly conductive electrode layers of negligible thickness covering the top and bottom surfaces of the piezoceramic patch. It is assumed that the piezoelectric volume is much smaller than the host structure so the patch is coupled to the host only electromechanically (with negligible mass and stiffness contribution).

For a thin piezoceramic patch attached on the host plate, the linear piezoelectric constitutive equations can be written as [48]

$$\begin{bmatrix} T_1^P \\ T_2^P \\ T_6^P \\ D_3 \end{bmatrix} = \begin{bmatrix} \bar{c}_{11}^E & \bar{c}_{12}^E & 0 & -\bar{e}_{31} \\ \bar{c}_{12}^E & \bar{c}_{22}^E & 0 & -\bar{e}_{31} \\ 0 & 0 & \bar{c}_{66}^E & 0 \\ \bar{e}_{31} & \bar{e}_{31} & 0 & \bar{\epsilon}_{33}^S \end{bmatrix} \begin{bmatrix} S_1^P \\ S_2^P \\ S_6^P \\ E_3 \end{bmatrix} \quad (1)$$

where  $T_1^P$  and  $T_2^P$  are the normal stress components along  $x$  and  $y$  axes respectively,  $T_6^P$  is the shear stress in the  $x$ - $y$  plane,  $D_3$  is the electric displacement in  $z$  direction (poling direction of piezoceramic patch),  $S_1^P$  and  $S_2^P$  are the normal strain components along the  $x$  and  $y$  axes,  $S_6^P$  is the shear strain component in the  $x$ - $y$  plane, and  $E_3$  is the electric field in the thickness direction. The effective piezoelectric stress constant is  $\bar{e}_{31}$ , elastic stiffness components are  $\bar{c}_{11}^E$ ,  $\bar{c}_{12}^E$  and  $\bar{c}_{66}^E$  (note that  $\bar{c}_{22}^E = \bar{c}_{11}^E$ ), and  $\bar{\epsilon}_{33}^S$  represents the permittivity component. Superscript P represents the piezoceramic patch, while  $E$  and  $S$  denote that the respective parameters are evaluated at constant electric field and constant strain, respectively. The over-bar denotes that the respective parameter is reduced to two-dimensional (2D) form from three-dimensional (3D)

electroelasticity components based on the following relations

$$\begin{aligned} \bar{c}_{11}^E &= \frac{s_{11}^E}{(s_{11}^E + s_{12}^E)(s_{11}^E - s_{12}^E)} \\ \bar{c}_{12}^E &= \frac{-s_{12}^E}{(s_{11}^E + s_{12}^E)(s_{11}^E - s_{12}^E)} \\ \bar{c}_{66}^E &= \frac{1}{s_{66}^E} \quad \bar{e}_{31} = \frac{d_{31}}{s_{11}^E + s_{12}^E} \quad \bar{\epsilon}_{33}^S = \epsilon_{33}^T - \frac{2d_{31}^2}{s_{11}^E + s_{12}^E} \end{aligned} \quad (2)$$

where  $s_{11}^E$ ,  $s_{12}^E$  and  $s_{66}^E$  are elastic compliance parameters at constant electric field  $E$ ,  $d_{31}$  is the piezoelectric strain constant, and  $\epsilon_{33}^T$  is the permittivity component at constant stress  $T$ .

The partial differential equation governing the forced vibrations of a thin plate with a small piezoceramic patch can be written as

$$\begin{aligned} \frac{\partial^2(M_1^S + M_1^P)}{\partial x^2} + 2 \frac{\partial^2(M_6^S + M_6^P)}{\partial x \partial y} + \frac{\partial^2(M_2^S + M_2^P)}{\partial y^2} \\ - c \frac{\partial w(x, y, t)}{\partial t} - \rho_s h_s \frac{\partial^2 w(x, y, t)}{\partial t^2} \\ + f(t) \delta(x - x_0) \delta(y - y_0) = 0 \end{aligned} \quad (3)$$

where  $w(x, y, t)$  is transverse deflection of the plate at position  $(x, y)$  and time  $t$ . The internal bending moments are  $M_1$ ,  $M_2$  and  $M_6$  while superscripts S and P stand for the host structure and the piezoceramic patch, respectively. The mass density of the plate is  $\rho_s$  and  $c$  is the viscous damping coefficient. The transverse force  $f(t)$  is acting at  $(x_0, y_0)$ . The Dirac delta functions are  $\delta(x)$  and  $\delta(y)$  along the  $x$  and  $y$  directions. The internal bending moments of the host structure can be expressed in terms of curvatures as follows:

$$M_1^S = -D \left( \frac{\partial^2 w(x, y, t)}{\partial x^2} + \nu_s \frac{\partial^2 w(x, y, t)}{\partial y^2} \right) \quad (4)$$

$$M_2^S = -D \left( \frac{\partial^2 w(x, y, t)}{\partial y^2} + \nu_s \frac{\partial^2 w(x, y, t)}{\partial x^2} \right) \quad (5)$$

$$M_6^S = -D(1 - \nu_s) \frac{\partial^2 w(x, y, t)}{\partial x \partial y} \quad (6)$$

where the bending stiffness of the plate is  $D = Y_s h_s^3 / (12 - 12\nu_s^2)$ , while its Young's modulus and Poisson's ratio are  $Y_s$

and  $v_s$ . The internal moments of the piezoceramic patch are

$$M_1^P = [H(x - x_1) - H(x - x_2)][H(y - y_1) - H(y - y_2)] \times \int_p T_1^P z \, dz \quad (7)$$

$$M_2^P = [H(x - x_1) - H(x - x_2)][H(y - y_1) - H(y - y_2)] \times \int_p T_2^P z \, dz \quad (8)$$

$$M_6^P = [H(x - x_1) - H(x - x_2)][H(y - y_1) - H(y - y_2)] \times \int_p T_6^P z \, dz \quad (9)$$

where  $H(x)$  and  $H(y)$  are the Heaviside functions and the integrals are over the thickness of piezoceramic patch. Substituting internal moments of the host plate and the piezoceramic patch in equations (4)–(6) and (7)–(9) into equation (3), the governing partial differential equation of the plate with piezoelectric coupling is

$$D \left( \frac{\partial^4 w(x, y, t)}{\partial x^4} + 2 \frac{\partial^4 w(x, y, t)}{\partial x^2 \partial y^2} + \frac{\partial^4 w(x, y, t)}{\partial y^4} \right) + c \frac{\partial w(x, y, t)}{\partial t} + \rho_s h_s \frac{\partial^2 w(x, y, t)}{\partial t^2} - \theta v(t) \left\{ \left[ \frac{d\delta(x - x_1)}{dx} - \frac{d\delta(x - x_2)}{dx} \right] \times [H(y - y_1) - H(y - y_2)] + \left[ \frac{d\delta(y - y_1)}{dy} - \frac{d\delta(y - y_2)}{dy} \right] \times [H(x - x_1) - H(x - x_2)] \right\} = f(t)\delta(x - x_0)\delta(y - y_0) \quad (10)$$

where  $v(t)$  is the voltage across the external resistive load and the electromechanical term  $\theta$  is defined as  $\theta = \bar{e}_{31} h_{pc}$ , which is the multiplication of effective piezoelectric constant  $\bar{e}_{31}$  and reference distance  $h_{pc}$  of the center layer of the piezoceramic patch to the reference surface (i.e., the neural axis level of the plate) at the location of the patch. Note that the volume of the piezoceramic patch is assumed to be significantly smaller than the host plate, and the piezoceramic patch's inertial and stiffness effects are neglected. Equation (10) governs the mechanical motion of the host plate and the piezoceramic patch with electrical coupling. The governing differential equation of the electrical circuit is derived next.

The electric displacement in equation (1) is

$$D_3 = \bar{e}_{31} S_1^P + \bar{e}_{31} S_2^P + \bar{\epsilon}_{33}^S E_3 \quad (11)$$

where the electric field  $E_3$  can be defined in terms of the electrical potential difference  $v(t)$ , as  $E_3 = -v(t)/h_p$ , and the axial strain components ( $S_1^P$  and  $S_2^P$  along the  $x$  and  $y$  axes) at the center layer of piezoceramic patch are

$$S_1^P(x, y, t) = -h_{pc} \frac{\partial^2 w(x, y, t)}{\partial x^2} \quad (12)$$

$$S_2^P(x, y, t) = -h_{pc} \frac{\partial^2 w(x, y, t)}{\partial y^2}.$$

The electric current flowing to the resistive load can be obtained using

$$\frac{d}{dt} \int_A \mathbf{D} \cdot \mathbf{n} \, dA = \frac{v(t)}{R_1} \quad (13)$$

where  $\mathbf{n}$  is the unit vector outward from electrode surface,  $\mathbf{D}$  is the electric displacement vector and integral is over the electrode's surface area  $A$ . The inner product between the unit vector  $\mathbf{n}$  and the electric displacement  $\mathbf{D}$  vector results in electric displacement term  $D_3$ , which is in the normal direction of the electrode surface along the  $z$  axis. Hence, substituting equations (11) and (12) into equation (13), we obtain

$$\frac{d}{dt} \int_{y=y_1}^{y_2} \int_{x=x_1}^{x_2} \left[ -h_{pc} \bar{e}_{31} \left( \frac{\partial^2 w(x, y, t)}{\partial x^2} + \frac{\partial^2 w(x, y, t)}{\partial y^2} \right) - \bar{\epsilon}_{33}^S \frac{v(t)}{h_p} \right] dx \, dy = \frac{v(t)}{R_1} \quad (14)$$

and defining the capacitance of the piezoceramic patch as  $C_p = (\bar{\epsilon}_{33}^S w_p l_p) / h_p$  and electromechanical coupling term as  $\theta = \bar{e}_{31} h_{pc}$ , the following equation governs coupled electrical circuit dynamics:

$$C_p \frac{dv(t)}{dt} + \frac{v(t)}{R_1} + \theta \left\{ \int_{y=y_1}^{y_2} \int_{x=x_1}^{x_2} \left[ \frac{\partial^3 w(x, y, t)}{\partial x^2 \partial t} + \frac{\partial^3 w(x, y, t)}{\partial y^2 \partial t} \right] dx \, dy \right\} = 0. \quad (15)$$

Therefore, equations (10) and (15) represent the distributed-parameter electroelastic model of piezoceramic patch harvester in physical coordinates, and these equations can be solved using modal analysis.

## 2.2. Governing electroelastic equations in modal coordinates

Based on the standard modal analysis procedure, the vibration of a thin plate can be represented as

$$w(x, y, t) = \sum_{n=1}^{\infty} \sum_{m=1}^{\infty} \phi_{mn}(x, y) \eta_{mn}(t) \quad (16)$$

where mass-normalized eigenfunction is  $\phi_{mn}(x, y)$  and the modal time response is  $\eta_{mn}(t)$  for the  $m$ th vibration mode. The eigenfunctions of the undamped CCCC rectangular plate are obtained as [49]

$$\phi_{mn}(x, y) = \Theta_{mn} \left( \cos \lambda_{mn}^x x - \sigma_{mn}^x \sin \lambda_{mn}^x x - \cosh \mu_{mn}^x x + \frac{\lambda_{mn}^x}{\mu_{mn}^x} \sigma_{mn}^x \sinh \mu_{mn}^x x \right) \times \left( \cos \lambda_{mn}^y y - \sigma_{mn}^y \sin \lambda_{mn}^y y - \cosh \mu_{mn}^y y + \frac{\lambda_{mn}^y}{\mu_{mn}^y} \sigma_{mn}^y \sinh \mu_{mn}^y y \right) \quad (17)$$

where  $\sigma_{mn}^x$  and  $\sigma_{mn}^y$  are

$$\sigma_{mn}^x = \frac{\cos \lambda_{mn}^x a - \cosh \mu_{mn}^x a}{\sin \lambda_{mn}^x a - \frac{\lambda_{mn}^x}{\mu_{mn}^x} \sinh \mu_{mn}^x a} \quad (18)$$

$$\sigma_{mn}^y = \frac{\cos \lambda_{mn}^y b - \cosh \mu_{mn}^y b}{\sin \lambda_{mn}^y b - \frac{\lambda_{mn}^y}{\mu_{mn}^y} \sinh \mu_{mn}^y b}$$

and  $\Theta_{mn}$  is the modal amplitude constant, which can be evaluated by normalizing the eigenfunctions according to the following orthogonality conditions:

$$\int_0^b \int_0^a \rho_s h_s \phi_{mn}(x, y) \phi_{rs}(x, y) dx dy = \delta_{mr} \delta_{ns} \quad (19)$$

$$\int_0^b \int_0^a D \left( \frac{\partial^2 \phi_{mn}(x, y)}{\partial x^2} \frac{\partial^2 \phi_{rs}(x, y)}{\partial x^2} \right. \\ \left. + 2 \frac{\partial^2 \phi_{mn}(x, y)}{\partial x^2} \frac{\partial^2 \phi_{rs}(x, y)}{\partial y^2} \right. \\ \left. + \frac{\partial^2 \phi_{mn}(x, y)}{\partial y^2} \frac{\partial^2 \phi_{rs}(x, y)}{\partial y^2} \right) dx dy \\ = \omega_{mn}^2 \delta_{mr} \delta_{ns} \quad (20)$$

where  $\delta_{mr}$  and  $\delta_{ns}$  are Kronecker delta functions,  $\delta_{mr}$  is equal to unity for  $m = r$ , and zero for  $m \neq r$ . Similarly  $\delta_{ns}$  is equal to unity for  $n = s$  and zero for  $n \neq s$ . The undamped natural frequency  $\omega_{mn}$  for the  $m$ th vibration mode of the plate in short circuit conditions (as  $R_1 \rightarrow 0$ ) is then

$$\omega_{mn} = \sqrt{\frac{\kappa_{mn}^4 D}{\rho_s h_s}} \quad (21)$$

where  $\kappa_{mn}$  is the frequency parameter of the undamped plate. The eigenvalues  $(\lambda_{mn}^x, \lambda_{mn}^y, \mu_{mn}^x, \mu_{mn}^y)$  can be obtained from the solution of the transcendental characteristic equations [49]:

$$\frac{1 - \cosh \mu_{mn}^x a \cos \lambda_{mn}^x a}{\sinh \mu_{mn}^x a \sin \lambda_{mn}^x a} = \frac{(\lambda_{mn}^x)^2 - (\mu_{mn}^x)^2}{2\lambda_{mn}^x \mu_{mn}^x} \quad (22)$$

$$\frac{1 - \cosh \mu_{mn}^y b \cos \lambda_{mn}^y b}{\sinh \mu_{mn}^y b \sin \lambda_{mn}^y b} = \frac{(\lambda_{mn}^y)^2 - (\mu_{mn}^y)^2}{2\lambda_{mn}^y \mu_{mn}^y} \quad (23)$$

$$\kappa_{mn} = \sqrt{(\lambda_{mn}^x)^2 + (\lambda_{mn}^y)^2} \quad (24)$$

$$\mu_{mn}^y = \sqrt{2\kappa_{mn}^2 - (\lambda_{mn}^y)^2} \quad (25)$$

$$\mu_{mn}^x = \sqrt{2\kappa_{mn}^2 - (\lambda_{mn}^x)^2} \quad (26)$$

for the intervals of

$$\lambda_{mn}^x a \in \left[ m\pi, m\pi + \frac{\pi}{2} \right], \quad m = 1, 2, \dots \quad (27)$$

$$\lambda_{mn}^y b \in \left[ n\pi, n\pi + \frac{\pi}{2} \right], \quad n = 1, 2, \dots$$

By following the modal analysis procedure [50] for a two-dimensional structure (multiplying partial differential equations in physical coordinates by eigenfunction  $\phi_{rs}(x, y)$  and integrating over the surface area of the plate), the following

electromechanically coupled ordinary differential equations for the modal time response  $\eta_{mn}$  can be obtained:

$$\frac{d^2 \eta_{mn}(t)}{dt^2} + 2\zeta_{mn} \omega_{mn} \frac{d\eta_{mn}(t)}{dt} \\ + \omega_{mn}^2 \eta_{mn}(t) - \tilde{\theta}_{mn} v(t) = f_{mn}(t). \quad (28)$$

Here,  $\omega_{mn}$  is the undamped natural frequency for the  $m$ th vibration mode. The modal damping ratio  $\zeta_{mn}$  can be obtained by using the damping identification techniques [51]. The modal forcing in equation (28) is

$$f_{mn} = \int_0^b \int_0^a f(t) \delta(x - x_0) \delta(y - y_0) \phi_{mn}(x, y) dx dy \\ = f(t) \phi_{mn}(x_0, y_0) \quad (29)$$

while the electromechanical coupling term  $\tilde{\theta}_{mn}$  can be given by

$$\tilde{\theta}_{mn} = \theta \left[ \int_{y_1}^{y_2} \frac{\partial \phi_{mn}(x, y)}{\partial x} \Big|_{x_1}^{x_2} dy + \int_{x_1}^{x_2} \frac{\partial \phi_{mn}(x, y)}{\partial y} \Big|_{y_1}^{y_2} dx \right]. \quad (30)$$

Hence, the slope of mode shapes  $\phi_{mn}$  along the edges of the piezoceramic patch together with the region covered determines the electromechanical coupling term. The modal expansion given by equation (16) can be substituted into the first-order differential equation governing electrical circuit (see equation (15)) to obtain

$$C_p \frac{dv(t)}{dt} + \frac{v(t)}{R_1} + \theta \sum_{n=1}^{\infty} \sum_{m=1}^{\infty} \left\{ \int_{y_1}^{y_2} \int_{x_1}^{x_2} \left( \frac{\partial^2 \phi_{mn}(x, y)}{\partial x^2} \right. \right. \\ \left. \left. + \frac{\partial^2 \phi_{mn}(x, y)}{\partial y^2} \right) \frac{d\eta_{mn}(t)}{dt} dx dy \right\} = 0. \quad (31)$$

Finally, the governing equation of electrical circuit can be written in modal coordinates as

$$C_p \frac{dv(t)}{dt} + \frac{v(t)}{R_1} + \sum_{n=1}^{\infty} \sum_{m=1}^{\infty} \tilde{\theta}_{mn} \frac{d\eta_{mn}(t)}{dt} = 0 \quad (32)$$

where  $v(t)$  is the voltage output across the resistive load  $R_1$ .

### 3. Steady-state response to harmonic excitation

#### 3.1. Closed-form voltage output and vibration response expressions

The electroelastic equations for a piezoelectric energy harvester attached on a thin plate are given in physical coordinates in equations (10) and (15) and in modal coordinates in equations (28) and (32). If the transverse force acting on the surface of the plate is assumed to be harmonic in the form  $f(t) = F_0 e^{j\omega t}$  (where the amplitude of the force is  $F_0$ ,  $\omega$  is the excitation frequency) and assuming linear oscillations, the steady-state expressions for modal response  $\eta_{mn}(t)$  and voltage response  $v(t)$  across the resistive load can be expressed as

$$\eta_{mn}(t) = H_{mn} e^{j\omega t} \quad v(t) = V e^{j\omega t} \quad (33)$$

where  $H_{mn}$  and  $V$  are the complex amplitudes. Substituting these steady-state expressions into governing equations in modal coordinates (equations (28) and (32)), one can obtain

$$-\omega^2 H_{mn} e^{j\omega t} + j2\zeta_{mn}\omega_{mn} H_{mn} e^{j\omega t} + \omega_{mn}^2 H_{mn} e^{j\omega t} - \tilde{\theta}_{mn} V e^{j\omega t} = F_0 e^{j\omega t} \phi_{mn}(x_0, y_0) \quad (34)$$

$$j\omega C_p V e^{j\omega t} + \frac{V e^{j\omega t}}{R_1} + e^{j\omega t} \sum_{n=1}^{\infty} \sum_{m=1}^{\infty} j\omega \tilde{\theta}_{mn} H_{mn} = 0 \quad (35)$$

and by eliminating  $e^{j\omega t}$  in equation (34),  $H_{mn}$  can be expressed as

$$H_{mn} = \frac{F_0 \phi_{mn}(x_0, y_0) + \tilde{\theta}_{mn} V}{\omega_{mn}^2 - \omega^2 + j2\zeta_{mn}\omega_{mn}\omega}. \quad (36)$$

Then, substitution of  $H_{mn}$  into equation (35) gives the voltage amplitude  $V$  as

$$V = \frac{-j\omega \sum_{n=1}^{\infty} \sum_{m=1}^{\infty} \frac{F_0 \phi_{mn}(x_0, y_0) \tilde{\theta}_{mn}}{\omega_{mn}^2 - \omega^2 + j2\zeta_{mn}\omega_{mn}\omega}}{j\omega C_p + \frac{1}{R_1} + \sum_{n=1}^{\infty} \sum_{m=1}^{\infty} \frac{j\omega \tilde{\theta}_{mn}^2}{\omega_{mn}^2 - \omega^2 + j2\zeta_{mn}\omega_{mn}\omega}}. \quad (37)$$

Hence, the steady-state voltage response  $v(t)$  across the resistive load is

$$v(t) = V e^{j\omega t} = \frac{-j\omega \sum_{n=1}^{\infty} \sum_{m=1}^{\infty} \frac{F_0 \phi_{mn}(x_0, y_0) \tilde{\theta}_{mn}}{\omega_{mn}^2 - \omega^2 + j2\zeta_{mn}\omega_{mn}\omega}}{j\omega C_p + \frac{1}{R_1} + \sum_{n=1}^{\infty} \sum_{m=1}^{\infty} \frac{j\omega \tilde{\theta}_{mn}^2}{\omega_{mn}^2 - \omega^2 + j2\zeta_{mn}\omega_{mn}\omega}} e^{j\omega t}. \quad (38)$$

Using the closed-form steady-state expression of the voltage across the resistive load in equation (38), the current  $i(t)$  and instantaneous power output  $P(t)$  generated by piezoceramic patch can be calculated by employing

$$i(t) = \frac{v(t)}{R_1} \quad P(t) = \frac{v^2(t)}{R_1}. \quad (39)$$

For the transverse deflection of the plate, the voltage amplitude  $V$  in equation (37) can be substituted in equation (36) and the expressions in equations (16) and (33) can be used to obtain

$$w(x, y, t) = \sum_{n=1}^{\infty} \sum_{m=1}^{\infty} \left( \phi_{mn}(x_0, y_0) - \frac{j\omega \tilde{\theta}_{mn} \sum_{n=1}^{\infty} \sum_{m=1}^{\infty} \frac{F_0 \phi_{mn}(x_0, y_0) \tilde{\theta}_{mn}}{\omega_{mn}^2 - \omega^2 + j2\zeta_{mn}\omega_{mn}\omega}}{j\omega C_p + \frac{1}{R_1} + \sum_{n=1}^{\infty} \sum_{m=1}^{\infty} \frac{j\omega \tilde{\theta}_{mn}^2}{\omega_{mn}^2 - \omega^2 + j2\zeta_{mn}\omega_{mn}\omega}} \right) \times \frac{F_0 \phi_{mn}(x, y) e^{j\omega t}}{\omega_{mn}^2 - \omega^2 + j2\zeta_{mn}\omega_{mn}\omega}. \quad (40)$$

Closed-form steady-state expressions for voltage output and vibration responses have been derived for the CCCC plate; however, it should be noted that these analytical expressions are applicable to different boundary conditions of host plates using the respective modal parameters (natural frequencies  $\omega_{mn}$ , eigenfunctions  $\phi_{mn}$  and damping ratios  $\zeta_{mn}$ ).

### 3.2. Multi-mode and single-mode electroelastic FRFs

Closed-form steady-state expressions for electrical voltage output and vibration response are derived in the former section. Using these steady-state expressions, two multi-mode FRFs can be extracted between two outputs and one input (voltage output-to-transverse force excitation and displacement-to-transverse force excitation). The voltage FRF relating the voltage output to point force input can be given by

$$\alpha(\omega) = \frac{v(t)}{F_0 e^{j\omega t}} = \frac{-j\omega \sum_{n=1}^{\infty} \sum_{m=1}^{\infty} \frac{\phi_{mn}(x_0, y_0) \tilde{\theta}_{mn}}{\omega_{mn}^2 - \omega^2 + j2\zeta_{mn}\omega_{mn}\omega}}{j\omega C_p + \frac{1}{R_1} + \sum_{n=1}^{\infty} \sum_{m=1}^{\infty} \frac{j\omega \tilde{\theta}_{mn}^2}{\omega_{mn}^2 - \omega^2 + j2\zeta_{mn}\omega_{mn}\omega}} \quad (41)$$

and the displacement FRF relating the transverse displacement to point force input is

$$\beta(x, y, \omega) = \frac{w(x, y, t)}{F_0 e^{j\omega t}} = \sum_{n=1}^{\infty} \sum_{m=1}^{\infty} \left( \frac{\phi_{mn}(x_0, y_0) - \frac{j\omega \tilde{\theta}_{mn} \sum_{n=1}^{\infty} \sum_{m=1}^{\infty} \frac{\phi_{mn}(x_0, y_0) \tilde{\theta}_{mn}}{\omega_{mn}^2 - \omega^2 + j2\zeta_{mn}\omega_{mn}\omega}}{j\omega C_p + \frac{1}{R_1} + \sum_{n=1}^{\infty} \sum_{m=1}^{\infty} \frac{j\omega \tilde{\theta}_{mn}^2}{\omega_{mn}^2 - \omega^2 + j2\zeta_{mn}\omega_{mn}\omega}}}{\omega_{mn}^2 - \omega^2 + j2\zeta_{mn}\omega_{mn}\omega}} \right) \times \phi_{mn}(x, y). \quad (42)$$

For excitation close to a resonance frequency, these two FRFs can be also simplified for a single mode as

$$\hat{\alpha}(\omega) = \frac{-j\omega R_1 \phi_{mn}(x_0, y_0) \tilde{\theta}_{mn}}{(j\omega R_1 C_p + 1) (\omega_{mn}^2 - \omega^2 + j2\zeta_{mn}\omega_{mn}\omega) + j\omega R_1 \tilde{\theta}_{mn}^2} \quad (43)$$

$$\hat{\beta}(x, y, \omega) = \frac{(j\omega R_1 C_p + 1) \phi_{mn}(x_0, y_0) \phi_{mn}(x, y)}{(j\omega R_1 C_p + 1) (\omega_{mn}^2 - \omega^2 + j2\zeta_{mn}\omega_{mn}\omega) + j\omega R_1 \tilde{\theta}_{mn}^2} \quad (44)$$

where a hat (^) symbol denotes the single-mode frequency response function. This single-mode expression is only valid for excitation frequencies close to the natural frequency ( $\omega \approx \omega_{mn}$ ). Note that these multi-mode and single-mode FRF expressions can be used for different boundary conditions of thin host plates by using their respective modal parameters.

## 4. Electroelastic analysis and experimental validations

### 4.1. Electroelastic analysis of structurally integrated piezoelectric energy harvester on thin plate

The dynamic strain distribution under the piezoceramic patch has significant effects on the performance of the collected charge output on the electrodes of the harvester. If the sign of the strain distribution changes under the area of piezoceramic

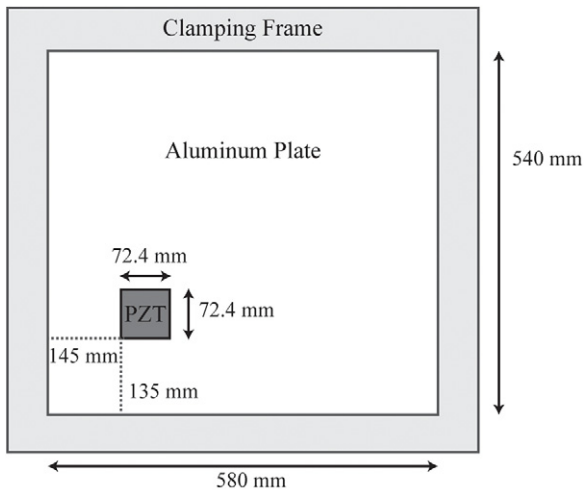


**Figure 2.** Position of the piezoceramic patch on the host plate with clamped boundary conditions.

**Table 1.** Geometric, material and electroelastic properties.

Property	Aluminum	Piezoceramic
Length (mm)	580	72.4
Width (mm)	540	72.4
Thickness (mm)	1.96	0.267
Young's modulus (GPa)	70	66
Mass density ( $\text{kg m}^{-3}$ )	2700	7800
Piezoelectric constant $d_{31}$ ( $\text{pm V}^{-1}$ )	—	−190
Permittivity constant $\bar{\epsilon}_{33}^S$ ( $\text{nF m}^{-1}$ )	—	10.38

patch, strong cancellations may occur in a continuous electrode due to the integral of strain on the continuous electrode surface. Erturk *et al* [21] pointed out that segmented electrodes should be used in order to avoid cancellations. In the case of a structurally integrated piezoelectric energy harvester on a thin plate, the cancellation of voltage output is also a problem since the host plate has vibration modes with certain mode shapes (as given in equation (17)) and dynamic strain distributions. Therefore, in this section, mode shapes and strain distributions of the thin plate are analyzed with a case study, which can be used a guideline for the positioning of piezoelectric energy harvester on the thin plate. The case study includes a piezoceramic patch structurally integrated on a CCCC aluminum plate as seen in figure 2. The material, geometric, dielectric and electroelastic properties of the aluminum plate and piezoceramic patch are given in table 1.

The first four undamped natural frequencies and corresponding normalized mode shapes of the host plate in the case study are obtained and displayed in figure 3. Note that the location of the piezoceramic patch is shown in the figure with a gray square. The analytical fundamental ( $m = 1$  and  $n = 1$ ) natural frequency is 55.34 Hz and the corresponding mode shape is in-phase on the overall surface with a maximum deflection at the center in figure 3(a). However, as can be seen in figures 3(b)–(d), higher vibration modes have several in-phase and out-of-phase regions across the surface. The second mode ( $m = 2$  and  $n = 1$ ) has an undamped natural

frequency of 107.83 Hz, and has a nodal line along the center of the  $x$  axis (length of the plate). For the third mode ( $m = 1$  and  $n = 2$ ), the natural frequency is 117.83 Hz, and has a nodal line along the center of the  $y$  axis (width of the plate). The fourth mode ( $m = 2$  and  $n = 2$ ) has a natural frequency of 165.94 Hz and the nodal lines of this mode are along the center lines of the  $x$  and  $y$  axes.

To investigate the cancelation of power output, strain mode shapes can be obtained using the Laplace operator  $\nabla$  with the undamped mode shape  $\phi_{mn}(x, y)$  for  $m$ th vibration mode of the plate:

$$\nabla \phi_{mn}(x, y) = \frac{\partial^2 \phi_{mn}(x, y)}{\partial x^2} + \frac{\partial^2 \phi_{mn}(x, y)}{\partial y^2} \quad (45)$$

Using equation (45), these strain mode shapes (i.e., normalized strain fields) are obtained and presented for the first four modes of the case study in figure 4. Strain mode shapes have in-phase and out-of-phase regions even for the fundamental mode of the CCCC plate. The number of the in-phase and out-of-phase regions of strain mode shapes can be obtained via the derived formulation as  $m \times n + 2(m + n)$ . For instance, the first mode has five distinct in-phase and out-of-phase regions while the second mode has eight such regions. If a continuous electrode is placed on the locations where strain changes sign, strong cancellations may occur, yielding significant reduction of electrical output. Therefore, a careful investigation is required prior to bonding the piezoceramic patches to the thin plate. In our case study, the piezoceramic patch is placed at the left-lower quadrant of the plate to harvest energy from multiple vibration modes of the plate. It should also be recalled that the piezoelectric patch is assumed to be small and therefore its effect on the strain distribution and mode-shape characteristics is negligible.

#### 4.2. Experimental setup for the structurally integrated piezoelectric energy harvester

In the experimental setup presented in figure 5, the aluminum host plate is clamped at all four edges with thick aluminum structural bars. Screws in two rows are tightened for perfect clamped boundary condition with a torque wrench to establish zero deflection and zero slope symmetrically along all four edges of the host plate. An off-the-shelf piezoceramic patch (T105-A4E-602 from Piezo Systems, Inc.) is attached on the host plate. The aluminum plate is excited by an electromechanical shaker through a sine-sweep signal generated by a signal generator while a force transducer (PCB 208C01) is placed between the shaker's rod and plate to measure the input. The transverse vibration of the plate is measured with a laser vibrometer (Polytec PDV 100) by targeting the center of the piezoceramic patch. Resistive loads ranging from short-circuit to open-circuit conditions are connected to the electrode's terminals of the piezoceramic patch. The signal analyzer (in figure 5) is used to collect and analyze the signals from the force transducer, the laser vibrometer and the voltage across the resistive load. By defining the force transducer's output as the reference channel in the signal analyzer, the experimental FRFs including the velocity response-to-force input (velocity FRF—also known as the mobility FRF) and voltage output-to-force input (voltage FRF) are obtained.

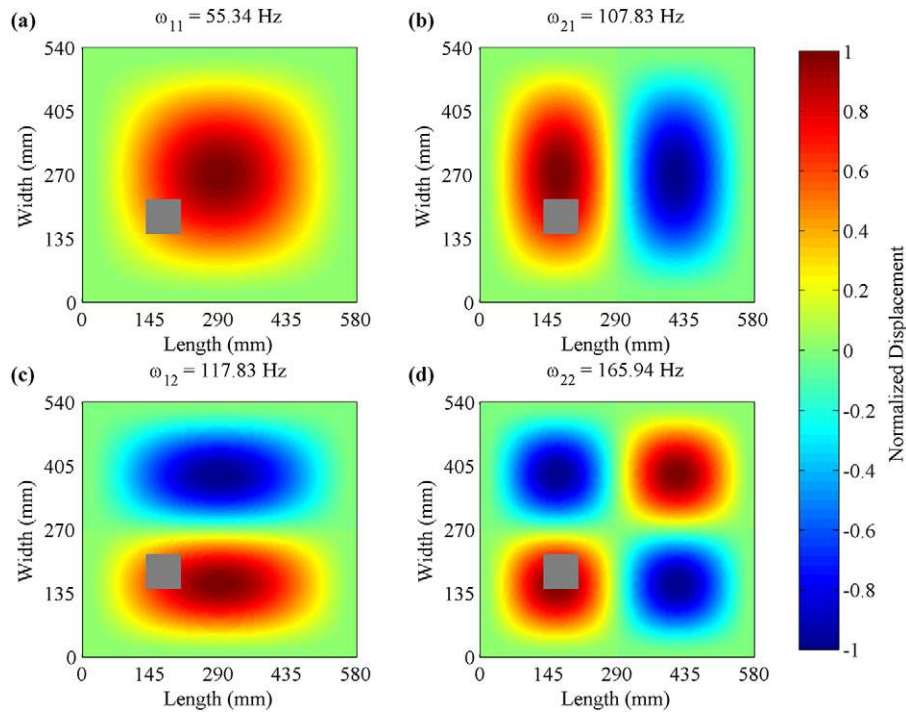


**Figure 3.** Normalized displacement fields for the (a) first, (b) second, (c) third, and (d) fourth modes of the CCCC plate analyzed in this work.

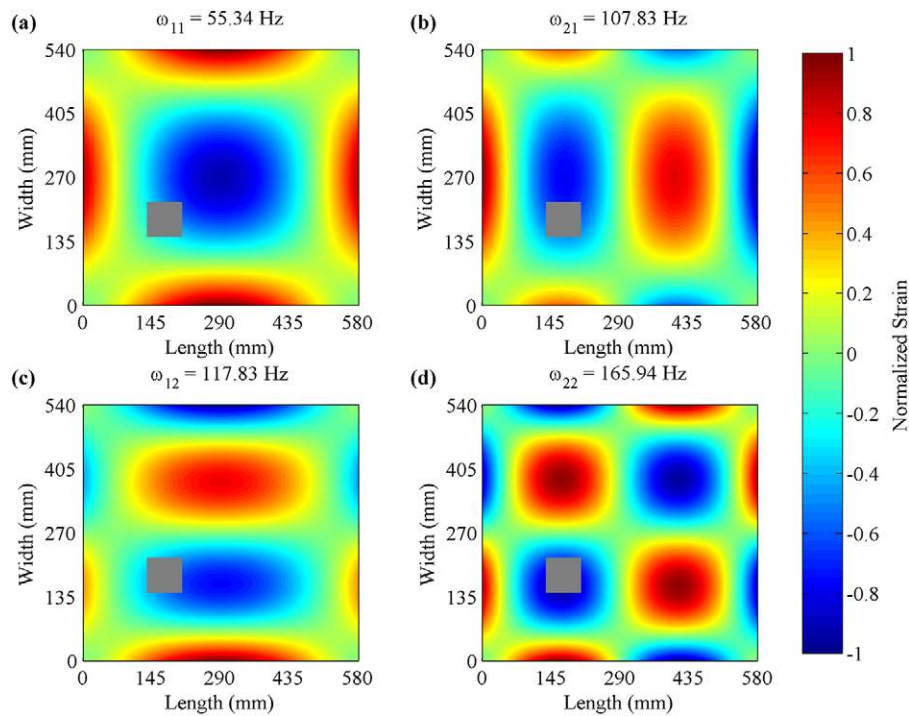


**Figure 4.** Normalized strain fields for the (a) first, (b) second, (c) third, and (d) fourth modes of the CCCC plate analyzed in this work.

**4.3. Experimental and analytical electroelastic velocity and voltage FRFs**

This section presents the analytical and experimental FRFs to demonstrate the accuracy of the analytical model. Note that in section 3, the analytical FRFs are obtained between

displacement of the plate and force input, whereas the velocity of the plate is measured using the laser vibrometer. Experimental velocity measurements can be integrated or analytical displacement FRFs can be differentiated for comparison. In this work, the analytical velocity FRFs are obtained simply multiplying analytical displacement FRFs with  $j\omega$ .



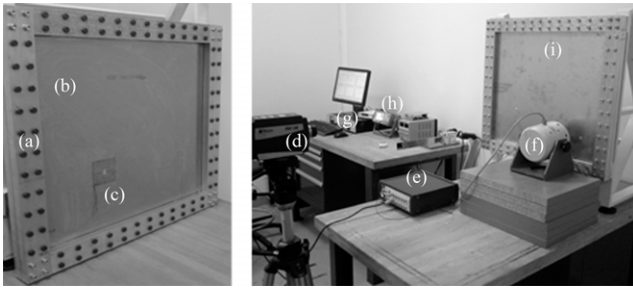


**Figure 5.** Details of the experimental setup: (a) clamping frame; (b) aluminum plate with piezoceramic patch; (c) piezoceramic patch; (d) laser vibrometer; (e) signal analyzer; (f) shaker; (g) amplifier; (h) signal generator; (i) aluminum plate without piezoceramic patch.

The mechanical damping ratios used in the analytical model are extracted from the experimental voltage FRF by applying the half-power point method at the resonance frequencies. Figures 6 and 7 present the analytical and experimental voltage and velocity FRFs for the moderate load resistance of 1.18 k $\Omega$ . As seen in these figures, the analytical velocity and voltage FRFs exhibit very good agreement with experimental results near the resonance and anti-resonance frequencies. The analytical model accurately predicts the velocity and voltage amplitudes for the first four modes of the host plate. At higher modes, there are small shifts at the resonance and anti-resonance frequencies, which may be due to experimental imperfections related to boundary conditions as well as material imperfections, however, the resonance and anti-resonance trends are still well predicted.

Having shown the accuracy of the analytical model with experimental FRF measurements for a moderate load resistance 1.18 k $\Omega$ , analytical and experimental voltage FRFs are obtained for a set of resistive loads consisting of 0.012, 0.058, 0.22, 0.464, 1.18, 2.83, 3.3, 5.49, 9.88, 14.6, 21.94, 32.48, 47.4, 100, 334.4, 479, 693, and 991 k $\Omega$ . In figure 8, the analytical voltage FRFs are given for these load resistance values. The voltage amplitude increases with increased load resistance up to a certain maximum voltage value around each resonance frequency. The maximum voltage amplitude differs for different resonance frequencies due to the positioning of

**Table 2.** The first four short-circuit and open-circuit resonance frequencies of the CCCC plate.

Resonance frequency (Hz)	Experiment	Analytical
$\omega_{11}^{sc}$ (short circuit)	56.54	55.34
$\omega_{11}^{oc}$ (open circuit)	57.03	55.40
$\omega_{21}^{sc}$ (short circuit)	104.69	107.83
$\omega_{21}^{oc}$ (open circuit)	105.47	108.10
$\omega_{12}^{sc}$ (short circuit)	116.99	117.83
$\omega_{12}^{oc}$ (open circuit)	117.68	118.10
$\omega_{22}^{sc}$ (short circuit)	160.84	165.94
$\omega_{22}^{oc}$ (open circuit)	161.52	166.60

the piezoelectric energy harvester on the plate (based on the strain mode shapes formerly discussed with figure 4). The experimental voltage FRFs for the set of resistive loads are presented in figure 9. The overall agreement between model predictions and experimental measurements is very good in figures 8 and 9.

#### 4.4. Experimental and analytical peak voltage, current, and power outputs

In this section, the peak electrical outputs (voltage, current and power) versus load resistance values are investigated. For this analysis, the experimental voltage FRFs are gathered for eighteen different resistive loads between 0.012 and 991 k $\Omega$  while the analytical voltage FRFs are obtained for one hundred resistive loads in the same range to have continuous curves. Note that, for each vibration mode, the analytical and experimental resonances move from short-circuit resonance frequency ( $\omega_{mn}^{sc}$  for  $R_1 \rightarrow 0$ ) to open-circuit resonance frequency ( $\omega_{mn}^{oc}$  for  $R_1 \rightarrow \infty$ ). The first four short-circuit and open-circuit resonance frequencies of the CCCC plate are listed in table 2. Using these analytical and experimental resonance frequencies, it is found that the maximum relative error of the analytical resonance frequency predictions is less than 3.2% in the first four modes.

The peak amplitudes versus resistive load trends are analyzed at the open-circuit resonance frequencies of the

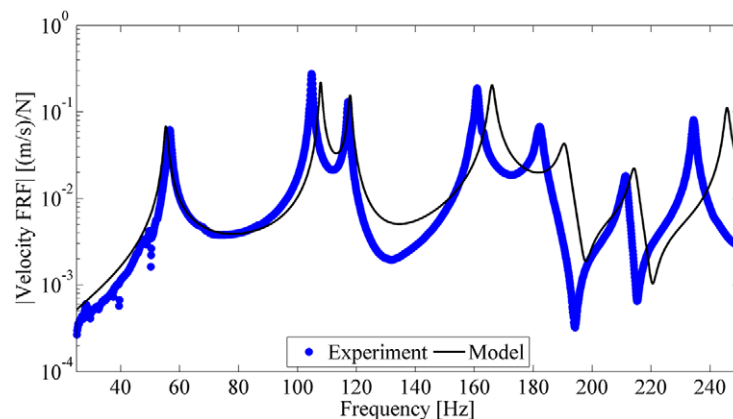


**Figure 6.** Comparison of the experimental and analytical velocity FRFs for a load resistance of 1.18 k $\Omega$ .

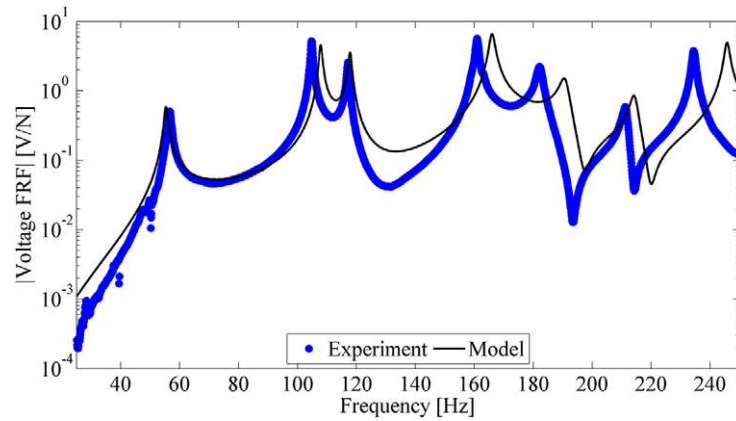


**Figure 7.** Comparison of the experimental and analytical voltage FRFs for a load resistance of 1.18 k $\Omega$ .

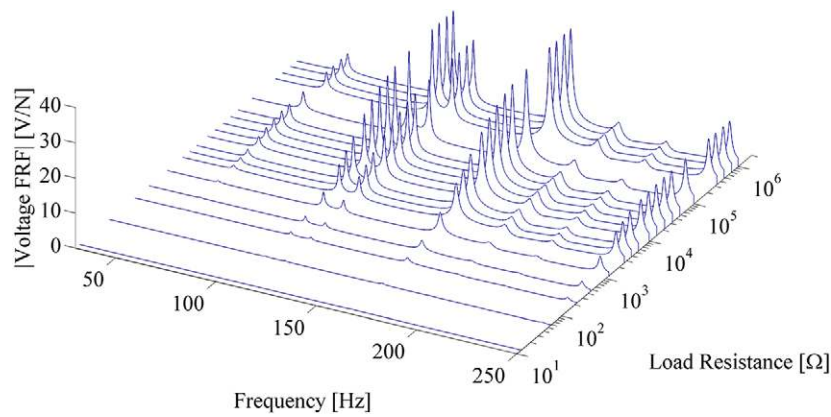


**Figure 8.** Analytical voltage FRFs for a set of resistive loads.

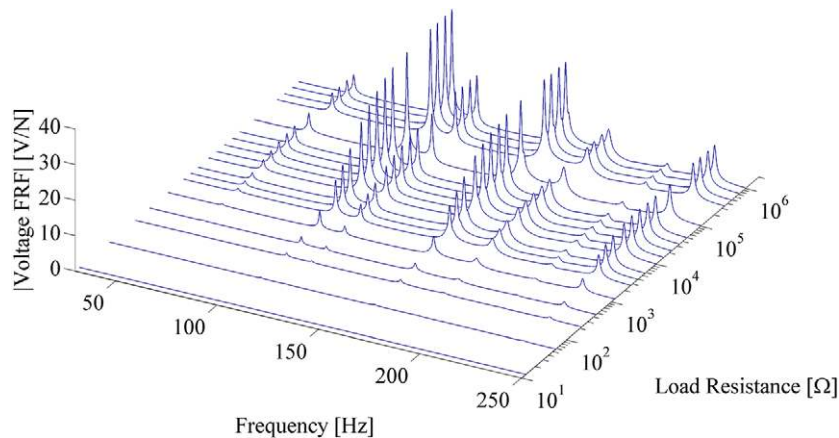


**Figure 9.** Experimental voltage FRFs for a set of resistive loads.

plate. Figure 10 presents the peak voltage amplitude versus load resistance graphs for the first four open-circuit resonance frequencies. As can be seen in this figure, the voltage across the resistive load at each resonance frequency increases monotonically up to a certain level and stays at this level in the limit  $R_l \rightarrow \infty$  (open-circuit condition). These peak voltage results show that the analytical voltage amplitudes have very

good agreement with the experimental results for a wide range of load resistance.

The current output flowing to the resistor is obtained by dividing the peak voltage amplitudes to load resistance values. Figure 11 shows the trend in the current generated by the piezoelectric energy harvester for the first four resonance frequencies. The current values monotonically decrease to

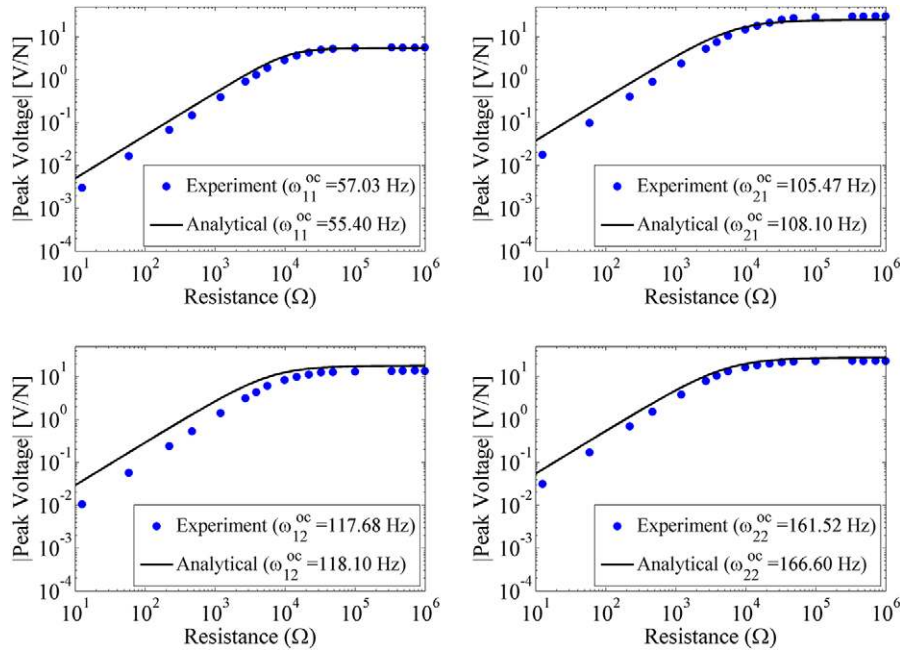


Figure 10. Variations of the voltage amplitude with load resistance for the first four vibration modes.

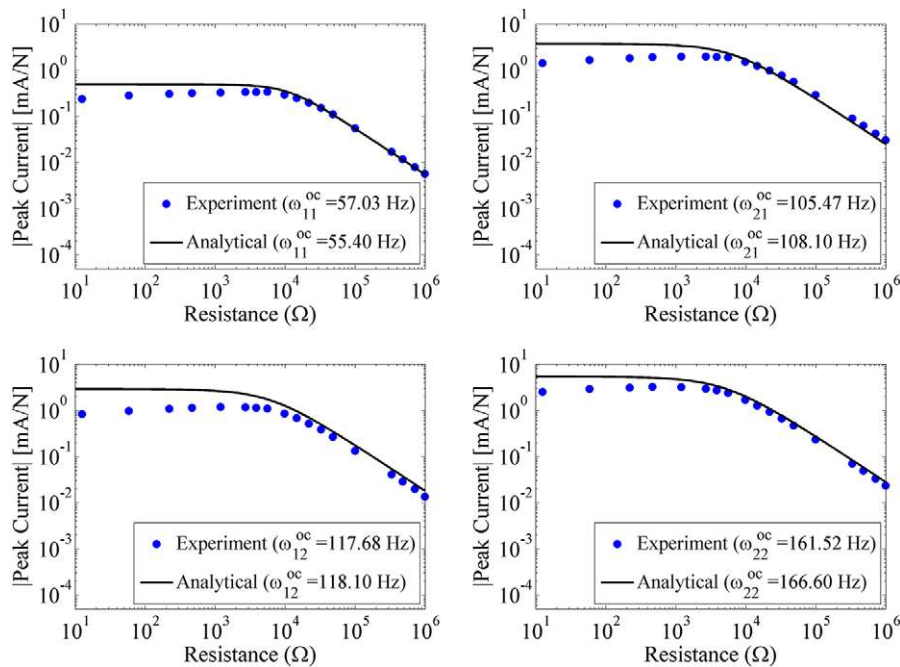


Figure 11. Variations of the current amplitude with load resistance for the first four vibration modes.

a zero value at open-circuit conditions from a certain level (maximum level) at short-circuit condition ( $R_1 \rightarrow 0$ ). The experimental trend in the current amplitude with varying load resistance is well captured by the analytical model. Mismatch in the low resistance region can be attributed to the level of noise in the measured electrical response for those resistive loads close to short-circuit condition.

Each resistive load results in different peak voltage and current amplitudes. Using the current and voltage amplitudes,

the electrical power output can be calculated for power output analysis. Figure 12 shows the trend of maximum power generated by the piezoelectric energy harvester with changing resistive load for the first four resonance frequencies. The variation of power output with changing load resistance yields a similar trend for each resonance frequency with different resistance values for the maximum output. It is useful to compare figures 12 and 4 with respect to the location of the piezoelectric patch relative to the strain nodes. In particular,

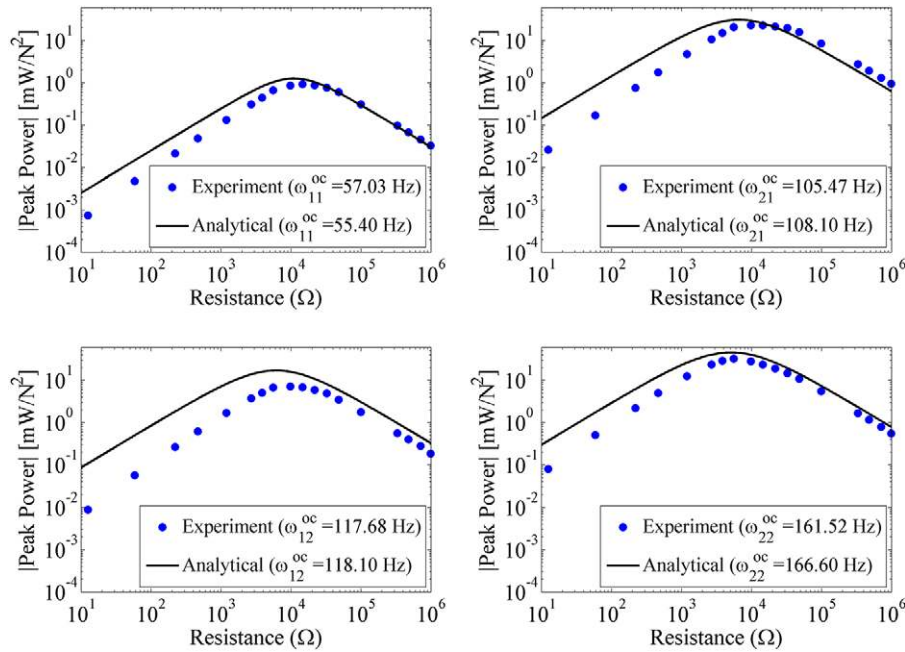


Figure 12. Variations of the peak power output with load resistance for the first four vibration modes.

the patch is located near a strain node curve in the fundamental vibration mode, and this mode indeed yields the lowest power output. For vibration modes that yield homogeneous strain field under the patch much larger power output can be extracted from the piezoelectric patch (compare the fourth vibration mode with others in figures 4 and 12 in terms of strain distribution and electrical power output, respectively). Therefore the optimal location of the piezoelectric patch constitutes an intriguing design problem for energy harvesting from multiple vibration modes of thin plates.

## 5. Conclusion

Structures made of thin plates with various boundary conditions are commonly used in aerospace, automotive, and marine applications. However, research on energy harvesting from vibrations of plate-like thin host structures has been very limited in the existing literature while cantilever-based configurations have been extensively explored. In this work, a distributed-parameter electroelastic model of a piezoelectric energy harvester structurally integrated to a thin plate was developed and presented. Closed-form steady-state solutions for the electrical output and structural response were derived for harmonic force inputs. Although the modeling and validations were given for fully clamped boundary conditions, the solution can be extended to other boundary conditions. Voltage and velocity FRFs were presented and experimentally verified with a case study for a range of external electrical load changing from short- to open-circuit conditions. The positioning of the piezoceramic patch was discussed for power generation from multiple vibration modes based on the mode-shape-dependent dynamic strain distribution. The electroelastic modeling framework presented herein can be utilized for optimal positioning of the harvesters on plate-like structures for multi-mode energy harvesting.

## Acknowledgment

The authors acknowledge the support of Koc University TUPRAS Energy Center (KUTEM).

## References

- [1] Roundy S, Wright P K and Rabaey J 2003 A study of low level vibrations as a power source for wireless sensor nodes *Comput. Commun.* **26** 1131–44
- [2] Beeby S P, Tudor M J and White N M 2006 Energy harvesting vibration sources for microsystems applications *Meas. Sci. Technol.* **17** R175–95
- [3] Paradiso J A and Starner T 2005 Energy scavenging for mobile and wireless electronics *IEEE Pervas. Comput.* **4** 18–27
- [4] Beeby S P et al 2007 A micro electromagnetic generator for vibration energy harvesting *J. Micromech. Microeng.* **17** 1257
- [5] Zhu D et al 2012 Vibration energy harvesting using the Halbach array *Smart Mater. Struct.* **21** 075020
- [6] Lee C et al 2009 Theoretical comparison of the energy harvesting capability among various electrostatic mechanisms from structure aspect *Sensors Actuators A* **156** 208–16
- [7] Chiu Y and Tseng V F G 2008 A capacitive vibration-to-electricity energy converter with integrated mechanical switches *J. Micromech. Microeng.* **18** 104004
- [8] Wang Z L and Song J 2006 Piezoelectric nanogenerators based on zinc oxide nanowire arrays *Science* **312** 242–6
- [9] Anton S R and Sodano H A 2007 A review of power harvesting using piezoelectric materials (2003–2006) *Smart Mater. Struct.* **16** R1–R21
- [10] Wang L and Yuan F G 2008 Vibration energy harvesting by magnetostrictive material *Smart Mater. Struct.* **17** 045009
- [11] Brufau-Penella J et al 2008 Characterization of the harvesting capabilities of an ionic polymer metal composite device *Smart Mater. Struct.* **17** 015009

- [12] Cook-Chennault K A, Thambi N and Sastry A M 2008 Powering MEMS portable devices—a review of non-regenerative and regenerative power supply systems with special emphasis on piezoelectric energy harvesting systems *Smart Mater. Struct.* **17** 043001
- [13] Erturk A and Inman D J 2008 A distributed parameter electromechanical model for cantilevered piezoelectric energy harvesters *J. Vib. Acoust.* **130** 041002
- [14] Elvin N G and Elvin A A 2009 A coupled finite element—circuit simulation model for analyzing piezoelectric energy generators *J. Intell. Mater. Syst. Struct.* **20** 587–95
- [15] Erturk A and Inman D J 2009 An experimentally validated bimorph cantilever model for piezoelectric energy harvesting from base excitations *Smart Mater. Struct.* **18** 025009
- [16] Yang Y and Tang L 2009 Equivalent circuit modeling of piezoelectric energy harvesters *J. Intell. Mater. Syst. Struct.* **20** 2223–35
- [17] Stanton S C *et al* 2012 Nonlinear nonconservative behavior and modeling of piezoelectric energy harvesters including proof mass effects *J. Intell. Mater. Syst. Struct.* **23** 183–99
- [18] Erturk A 2012 Assumed-modes modeling of piezoelectric energy harvesters: Euler–Bernoulli, Rayleigh, and Timoshenko models with axial deformations *Comput. Struct.* **106/107** 214–27
- [19] Zhao S and Erturk A 2013 Electroelastic modeling and experimental validations of piezoelectric energy harvesting from broadband random vibrations of cantilevered bimorphs *Smart Mater. Struct.* **22** 015002
- [20] Friswell M I and Adhikari S 2010 Sensor shape design for piezoelectric cantilever beams to harvest vibration energy *J. Appl. Phys.* **108** 014901
- [21] Erturk A *et al* 2009 Effect of strain nodes and electrode configuration on piezoelectric energy harvesting from cantilevered beams *J. Vib. Acoust.* **131** 011010
- [22] Erturk A, Bilgen O and Inman D J 2008 Power generation and shunt damping performance of a single crystal lead magnesium niobate-lead zirconate titanate unimorph: analysis and experiment *Appl. Phys. Lett.* **93** 224102
- [23] Lallart M and Guyomar D 2010 Piezoelectric conversion and energy harvesting enhancement by initial energy injection *Appl. Phys. Lett.* **97** 014104
- [24] Lien I C and Shu Y C 2012 Array of piezoelectric energy harvesting by the equivalent impedance approach *Smart Mater. Struct.* **21** 082001
- [25] Park J C, Khym S and Park J Y 2013 Micro-fabricated lead zirconate titanate bent cantilever energy harvester with multi-dimensional operation *Appl. Phys. Lett.* **102** 043901
- [26] Cottone F *et al* 2012 Piezoelectric buckled beams for random vibration energy harvesting *Smart Mater. Struct.* **21** 035021
- [27] Friswell M I *et al* 2012 Non-linear piezoelectric vibration energy harvesting from a vertical cantilever beam with tip mass *J. Intell. Mater. Syst. Struct.* **23** 1505–21
- [28] De Marqui C, Erturk A and Inman D J 2009 An electromechanical finite element model for piezoelectric energy harvester plates *J. Sound Vib.* **327** 9–25
- [29] De Marqui C, Erturk A and Inman D J 2010 Piezoaeroelastic modeling and analysis of a generator wing with continuous and segmented electrodes *J. Intell. Mater. Syst. Struct.* **21** 983–93
- [30] De Marqui C *et al* 2011 Modeling and analysis of piezoelectric energy harvesting from aeroelastic vibrations using the doublet-lattice method *J. Vib. Acoust.—Trans. ASME* **133** 011003
- [31] Rupp C J *et al* 2009 Design of piezoelectric energy harvesting systems: a topology optimization approach based on multilayer plates and shells *J. Intell. Mater. Syst. Struct.* **20** 1923–39
- [32] Erturk A 2011 Piezoelectric energy harvesting for civil infrastructure system applications: moving loads and surface strain fluctuations *J. Intell. Mater. Syst. Struct.* **22** 1959–73
- [33] Forward R L 1979 Electronic damping of vibrations in optical structures *Appl. Opt.* **18** 690–7
- [34] Hagood N W and von Flotow A 1991 Damping of structural vibrations with piezoelectric materials and passive electrical networks *J. Sound Vib.* **146** 243–68
- [35] Hollkamp J J 1994 Multimodal passive vibration suppression with piezoelectric materials and resonant shunts *J. Intell. Mater. Syst. Struct.* **5** 49–57
- [36] Wu S-Y 1998 Method for multiple mode piezoelectric shunting with single pzt transducer for vibration control *J. Intell. Mater. Syst. Struct.* **9** 991–8
- [37] Koshigoe S and Murdock J W 1993 A unified analysis of both active and passive damping for a plate with piezoelectric transducers *J. Acoust. Soc. Am.* **93** 346–55
- [38] Saravanos D A 1999 Damped vibration of composite plates with passive piezoelectric-resistor elements *J. Sound Vib.* **221** 867–85
- [39] Behrens S, Moheimani S O R and Fleming A J 2003 Multiple mode current flowing passive piezoelectric shunt controller *J. Sound Vib.* **266** 929–42
- [40] Fein O M 2008 A model for piezo-resistive damping of two-dimensional structures *J. Sound Vib.* **310** 865–80
- [41] Moheimani S O R 2003 A survey of recent innovations in vibration damping and control using shunted piezoelectric transducers *IEEE Trans. Control Syst. Technol.* **11** 482–94
- [42] Fleming A J, Behrens S and Moheimani S O R 2000 Synthetic impedance for implementation of piezoelectric shunt-damping circuits *Electron. Lett.* **36** 1525–6
- [43] Fleming A J and Moheimani S O R 2003 Adaptive piezoelectric shunt damping *Smart Mater. Struct.* **12** 36
- [44] Corrêa de Godoy T and Areias Trindade M 2011 Modeling and analysis of laminate composite plates with embedded active–passive piezoelectric networks *J. Sound Vib.* **330** 194–216
- [45] Huang Y M and Hung S C 2011 Analytical study of an active piezoelectric absorber on vibration attenuation of a plate *J. Sound Vib.* **330** 361–73
- [46] Casadei F *et al* 2010 Broadband vibration control through periodic arrays of resonant shunts: experimental investigation on plates *Smart Mater. Struct.* **19** 015002
- [47] Makihara K, Onoda J and Minesugi K 2005 Low energy-consumption hybrid vibration suppression based on energy-recycling approach *AIAA J.* **43** (8) 1706–15
- [48] Erturk A and Inman D J 2011 *Piezoelectric Energy Harvesting* (Chichester: Wiley)
- [49] Xing Y F and Liu B 2009 New exact solutions for free vibrations of thin orthotropic rectangular plates *Compos. Struct.* **89** 567–74
- [50] Meirovitch L 2001 *Fundamentals of Vibration* International edn (Singapore: McGraw-Hill Higher Education) p 806
- [51] Erturk A and Inman D J 2011 Parameter identification and optimization in piezoelectric energy harvesting: analytical relations, asymptotic analyses, and experimental validations *Proc. Inst. Mech. Eng. I* **225** 485–96